Supporting Information for: Control over crystal size in vapour deposited metal-halide perovskite films

*Kilian B. Lohmann, Jay B. Patel, Mathias Uller Rothmann, Chelsea Q. Xia, Robert D. J. Oliver, Laura M. Herz, Henry J. Snaith, and Michael B. Johnston**

Department of Physics, University of Oxford, Clarendon Laboratory, Parks Road, OX1 3PU, United Kingdom

E-mail: michael.johnston@physics.ox.ac.uk

Table of Contents

1. Device fabrication

1.1 Bottom contact

TEC 15 fluorine-doped tin oxide (FTO) was cleaned by sonication in Decon 90 solution (1%vol), de-ionised water, acetone, and finally isopropyl alcohol. Immediately prior to deposition, the samples were cleaned in O_2-plasma for 5 minutes.

1.2 N-type contact layer

C_{60} fullerene (Alfa-Aeser) was thermally evaporated in a custom Lesker thermal evaporator chamber at 0.1 Å/s, for a typical thickness of 10 nm for devices. The rate was measured and kept constant using a gold-plated quartz microbalance, and a PID loop control software.

1.3 Perovskite absorber layer

CH_3NH_3I (Greatcell) (MAI) and PbI_2 (99.999% metal base, Sigma-Aldricht) are co-evaporated in a custom Lesker thermal evaporator chamber. Heating of the sources starts once the chamber pressure falls below 5e-6 mbar. During the subsequent evaporation, the pressure goes up to 1-2e-5 mbar. The PbI_2 rate was kept constant at 0.30 Å/s using a gold-plated quartz microbalance, while the MAI temperature was controlled such that the overall deposition rate as measured by a quartz microbalance located next to the sensor was 0.45 Å/s. This rate is henceforth denoted by "substrate rate". For a typical 420 nm deposition, this involved ramping the MAI temperature from 175.1 °C to 183 °C, for 1.1 g of MAI initially in the crucible. For thicker depositions, in order to match the sublimation dynamics of the thinner samples as much as possible, the amount of fresh MAI initially put in the crucible was increased according to a MAI sublimation rate of 0.05 mg/s, and the starting temperature decreased slightly.

During deposition, MAI is known to sublimate omnidirectionally and deposit on all surfaces of the vacuum chamber. To reduce contamination from MAI resublimated off the walls during a deposition, we regularly bake out both sources at 450 °C and the substrate at 150 °C, much higher than is reached during film deposition. During deposition, the temperature of the walls of the chamber is controlled to be 17 °C. Finally, the substrate rate should account for the total amount of MAI sublimed onto the substrate, including any that potentially gets resublimed off the wall.

1.4 P-type contact layer

Spiro-OMeTAD (spiro) (Lumtec) was dissolved in Chlorobenzene at a concentration of 81 mg/mL, with added lithium bis(trifluoromethanesulfonyl)imide (Li-TFSI) dissolved in 1-Butanol at a concentration of 170 mg/mL, and tert-butylpiridine (tBP). 40 µL of the solution was then spin-coated dynamically at 2000 rpm for 45 s. Before depositing the final electrode, the films were kept in a desiccator for 15-17 hours to oxidise the spiro.

1.5 Top contact

80 nm of Au was evaporated in a commercial Lesker nano36 chamber, at a rate of 0.8 – 2.5 Å/s, as monitored by a gold-plated quartz microbalance. The rate was gradually increased during the first 15 nm of the deposition, at which point the maximum and final rate of 2.5 Å/s was reached. A mask was used to create devices of area 0.0919 cm^2.

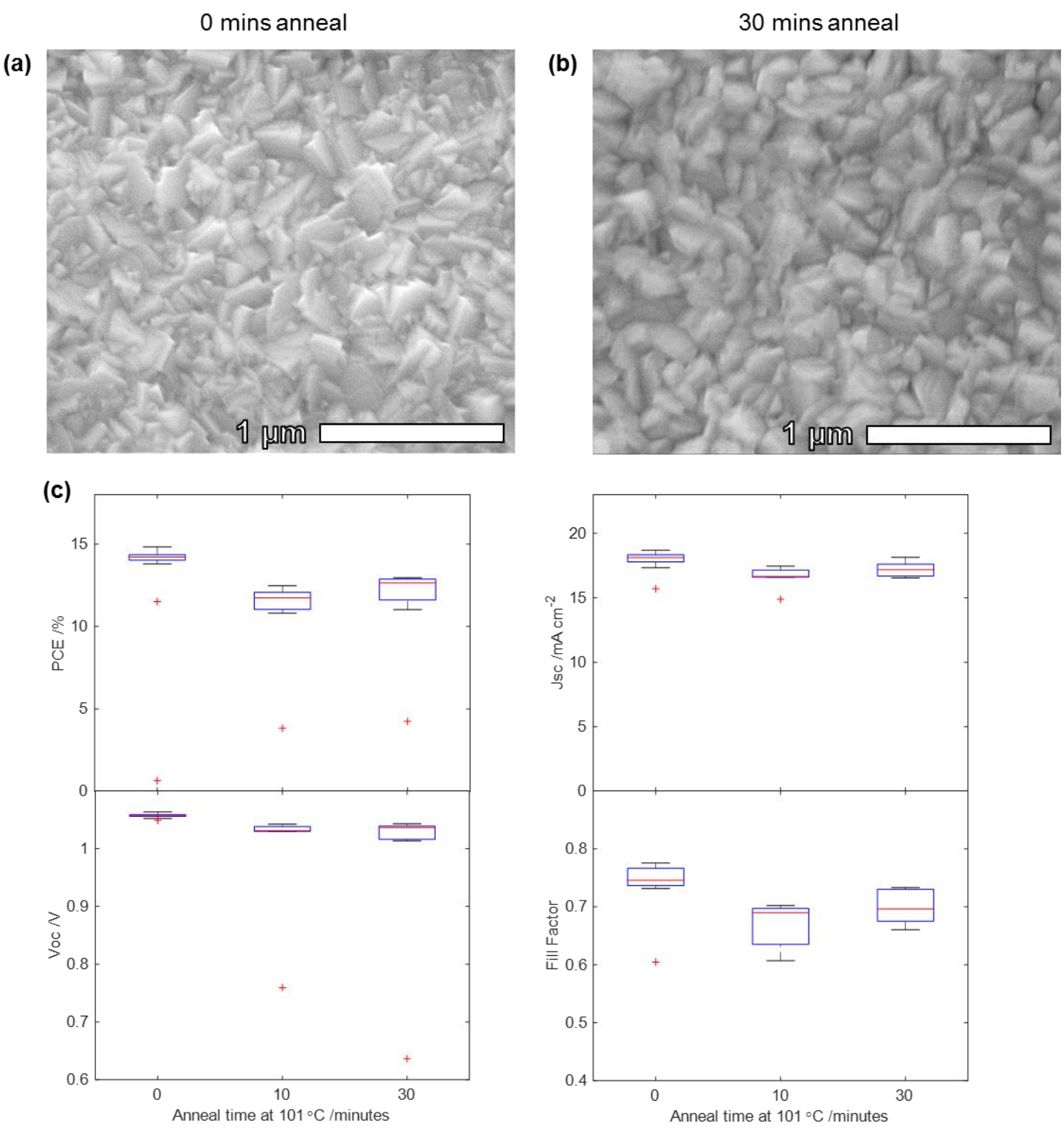

Figure S1: Top down SEM images of $CH_3NH_3PbI_3$ ($MAPbI_3$) films grown on FTO at substrate temperature 20°C for the first 60 nm, then 0°C for the remaining 440 nm **(a)** no post-deposition anneal **(b)** annealed for 30 minutes at 101°C **(c)** J-V characteristics for the corresponding devices

1.6 Annealing dependence

During the early stages of the study, films were annealed at 101°C prior to deposition of the p-type layer in hopes of inducing morphological changes. Not only were such changes not observed, but the performance also significantly decreased, as illustrated in Figure S1. As a result, the champion devices made later in the study, who's data was used in the main text, were not annealed. The data shown for Figure S1 comes from a run where the substrate temperature was changed from 20 °C for the first 60 nm to 0 °C for the remaining 440 nm.

1.7 Current voltage characterisation

Devices were measured using an ABET Technologies Sun 2000 and a Keithly 2400 sourcemeter at AM1.5 100 mW/cm^2 sunlight in ambient atmosphere. The lamp was calibrated with a KG5 Filtered silicon reference, itself calibrated by NREL. Using a mask, the active area for each device was 0.0919 cm^2, corresponding to the top contact area. The scan rate used was 0.3 V/s for both forward and reverse scans, with no initial stabilisation time, going from 0 – 1.2 V. The reverse scan was performed first, followed immediately by the forward scan. Stabilised characteristics were measured after 50 s of keeping the device at the voltage of the maximum power point, as determined by the JV scan.

2. Scanning electron microscopy

Top-down and cross-section images were taken using an FEI Quanta 600 FEG, at 5 keV and 10 keV acceleration voltage, respectively, with current defined by 2.5 spot size. The chamber was pumped down to high vacuum (< 2e-4 mbar).

The images in Figure S2 show that the inter-grain voids seen in the cross section of L in the main text (Figure 1b) originate from electron-beam damage during SEM image acquisition. This electron-induced damage is a well-known phenomenon, [1] [2] and depends exponentially on electron dose. [3] Figure S2a clearly shows the gaps are only present in regions subjected to a previous scan. The smaller red-boxed areas were imaged at a 5 times higher magnification, resulting in a 25 times higher electron dose per area, leading to exponentially more beam damage. Figure S2b shows that the voids must have originated after deposition of the spiro, lest the latter would have infiltrated down into the gaps.

The images shown in the main text represent small excerpts of the images taken. Larger versions of the cross-sections seen in Figure 1b and 1c are shown in Figure S3 for added clarity and detail. In addition, lower magnification images which show a larger area of the sample are shown in Figure S4 and S5 for cross-sections and top-down images, respectively.

(a)

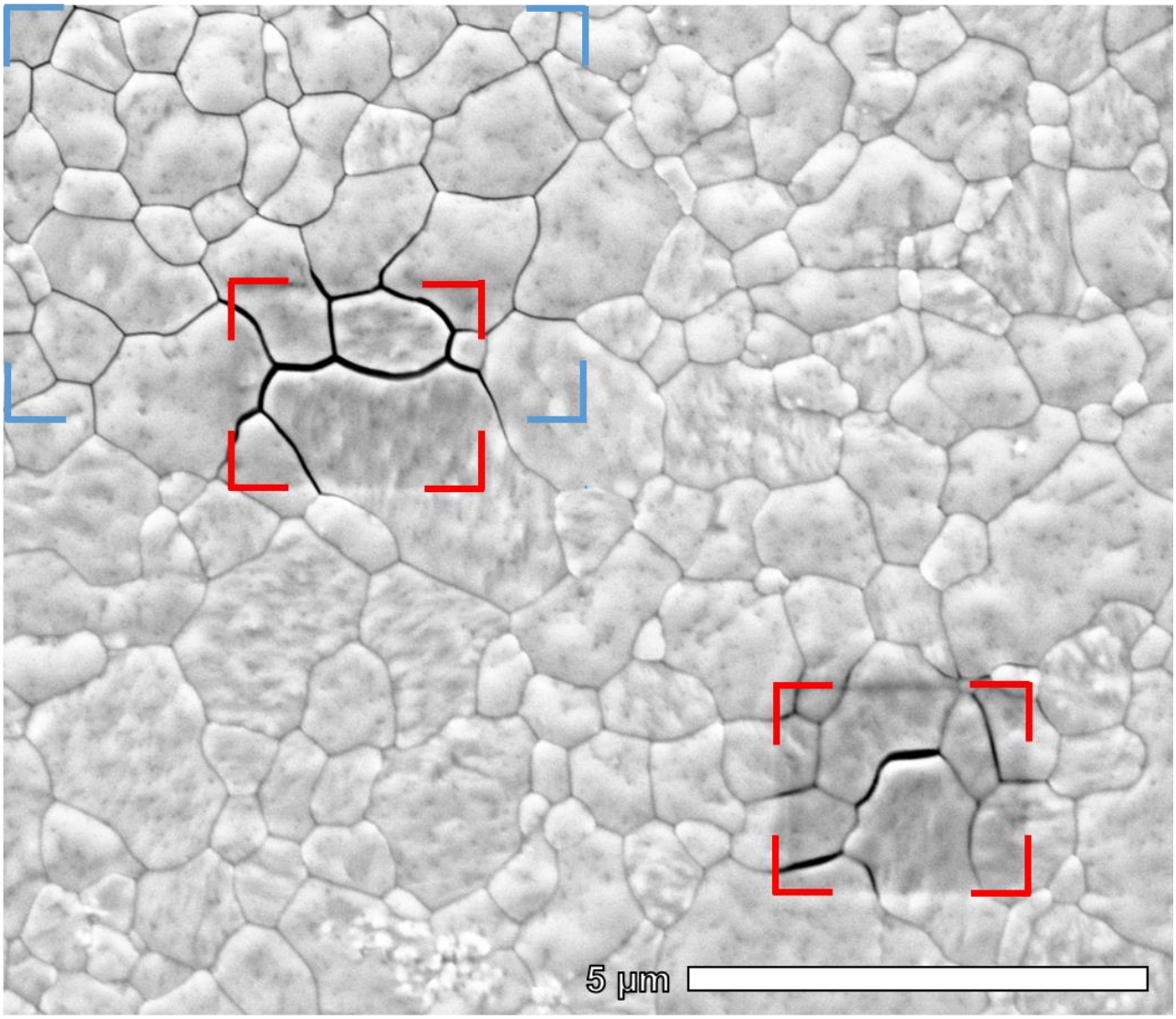

(b)

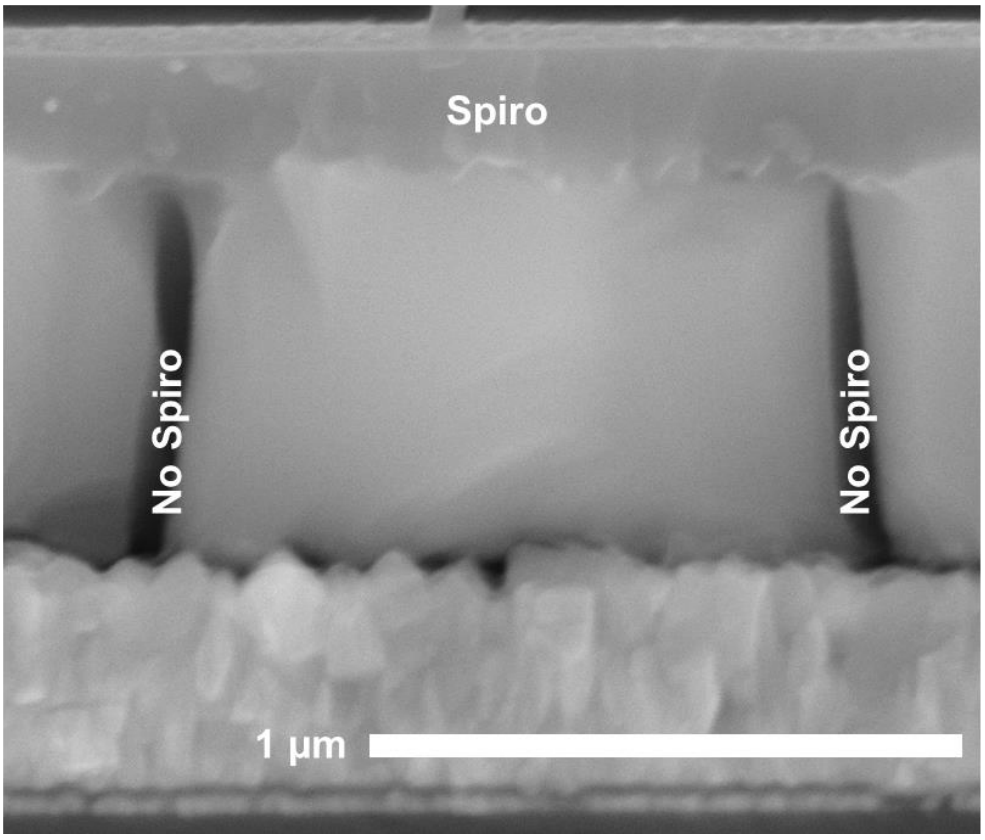

Figure S2: (a) SEM top down image of film L showing visible beam damage only in areas imaged previously, at the same magnification (blue rectangle) and 5 times higher magnification (red rectangles) **(b)** Close up of the SEM cross-section of L shown in Figure 1.b in the main text, showing clearly that no spiro has infiltrated down into the inter-grain voids.

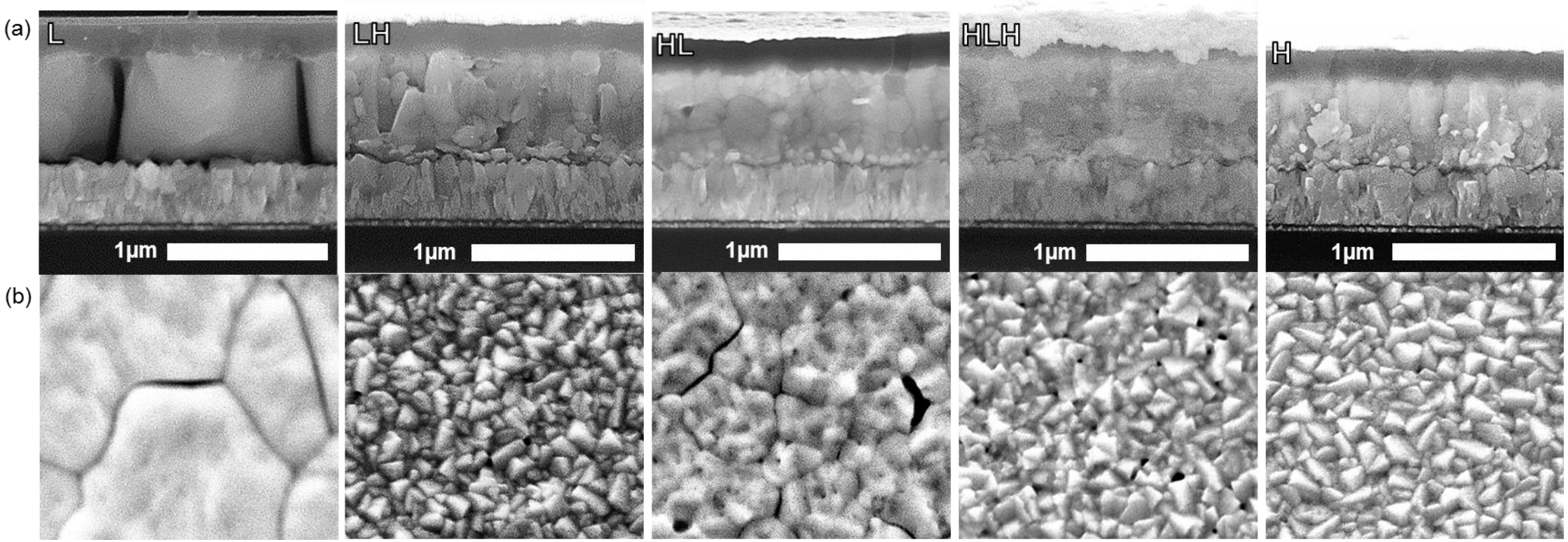

Figure S3: Larger size copies of the scanning electron microscope (SEM) images from Figure 1b and 1.c in the main text **(a)** Cross-sectional SEM images of co-evaporated $CH_3NH_3PbI_3$ ($MAPbI_3$) devices deposited at 5 different substrate temperature conditions L,LH,HL,HLH,H, as described in the main text. **(b)** Top-down SEM images of the same films.

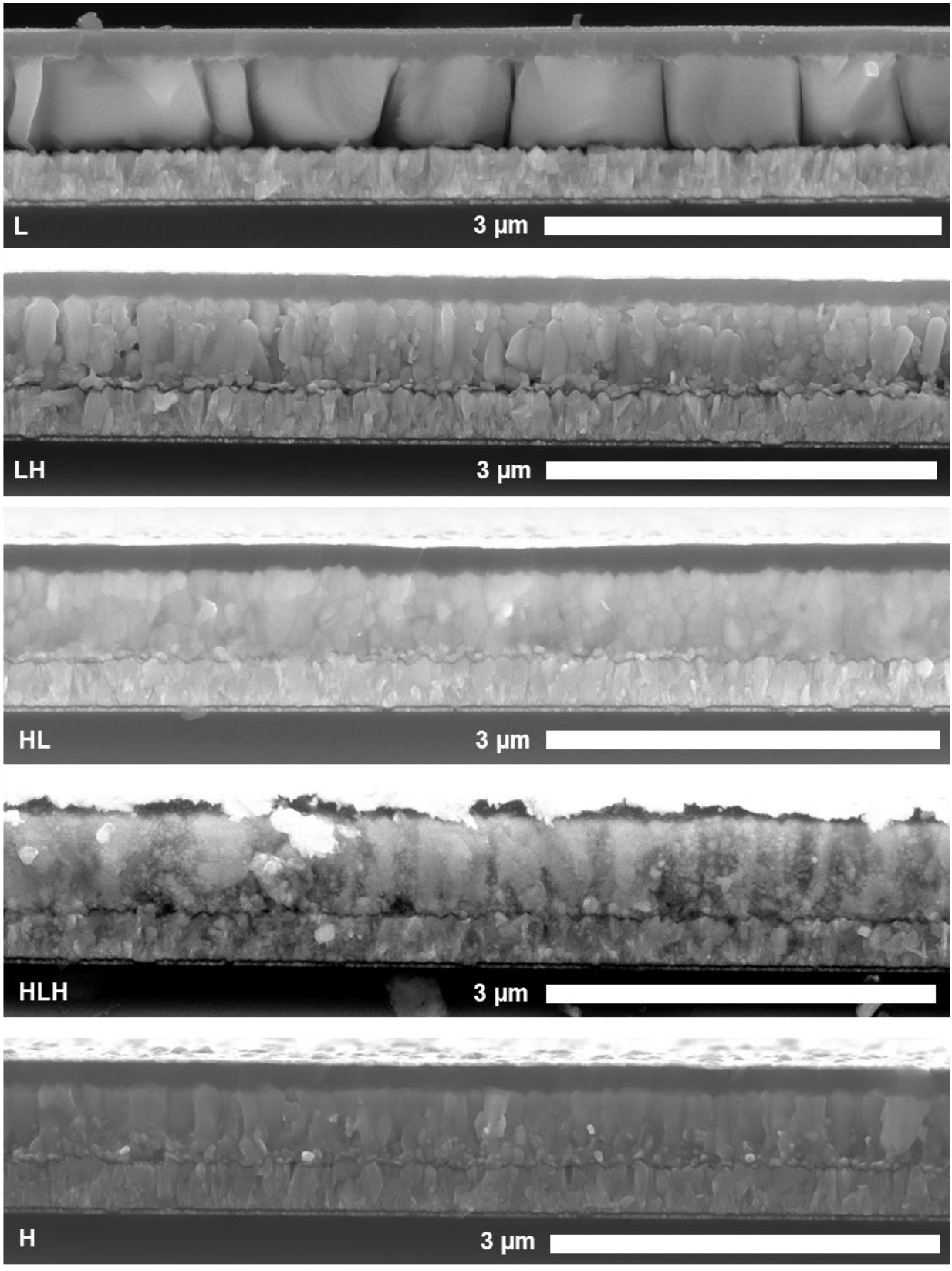

Figure S4: Cross-sectional scanning electron microscope images of co-evaporated $CH_3NH_3PbI_3$ ($MAPbI_3$) devices deposited at 5 different substrate temperature conditions L,LH,HL,HLH,H, as described in the main text.

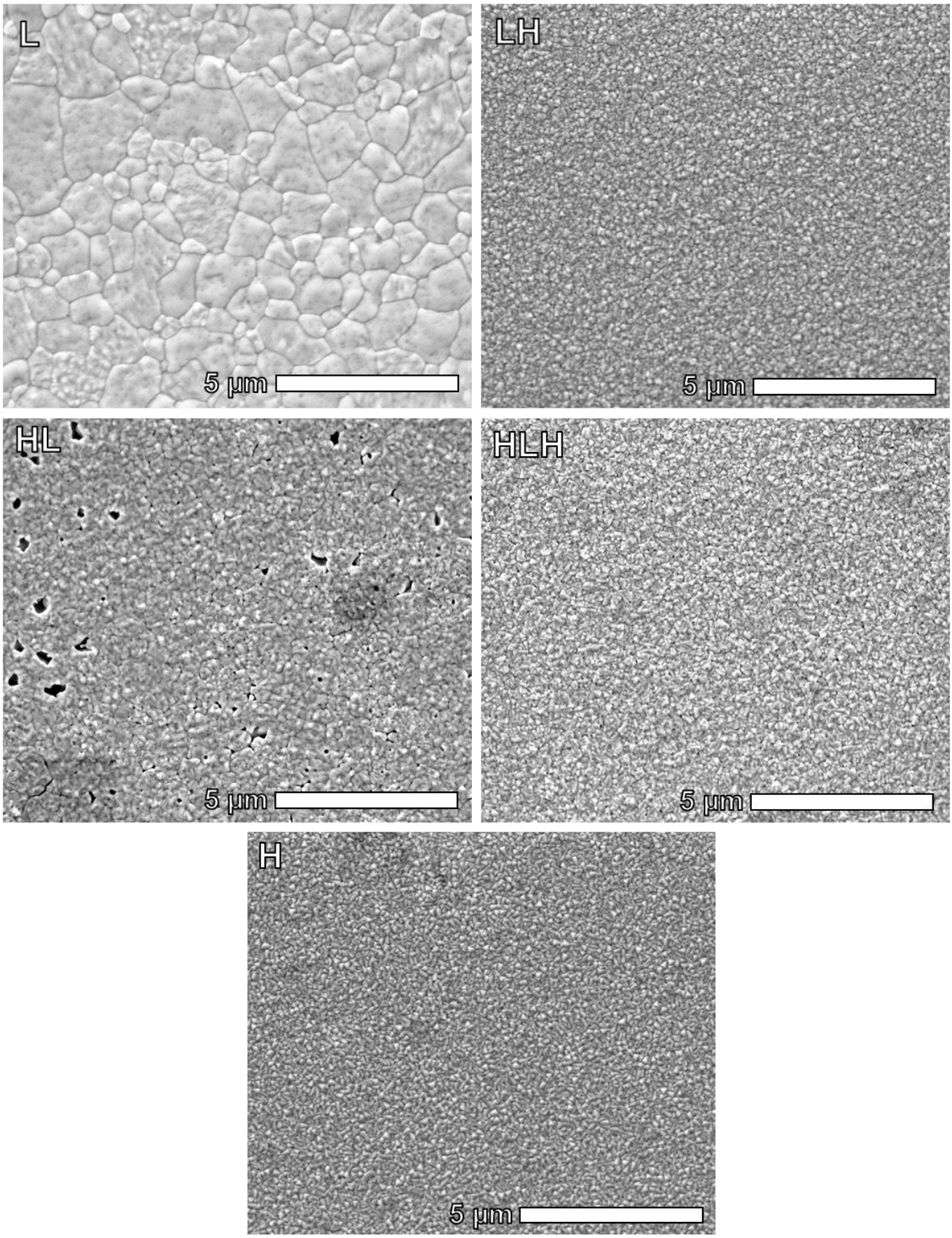

Figure S5: Top down view scanning electron microscope images of co-evaporated $CH_3NH_3PbI_3$ ($MAPbI_3$) devices deposited at 5 different substrate temperature conditions L,LH,HL,HLH,H, as described in the main text.

2.1 Morphology on different substrates

In addition to the FTO/C_{60}/$MAPbI_3$/Spiro/Au architecture used for the champion devices, we also tried Indium tin oxide (ITO)/C_{60}/$MAPbI_3$/Spiro/Au, and p-i-n devices with FTO/Poly[N,N'-bis(4-butylphenyl)-N,N'-bisphenylbenzidine] (PolyTPD)/$MAPbI_3$/C_{60}/Bathocuproine (BCP)/Au, as well as blank FTO and crystalline Si as substrates. Figure S6 shows the morphology across the different substrates. We only obtained large grains on FTO/C_{60}, and found the morphology very different on non-FTO substrates, with notably films grown on ITO showing much more columnar grains at low substrate temperatures. Nevertheless, device performance was also worse for ITO/C_{60} and FTO/PolyTPD, particularly for the latter, as shown in Figure S7. We believe that the main reason for this difference in performance, particularly between FTO/C_{60} and ITO/C_{60}, is due to a difference in the nucleation process. Because the C_{60} layer is only 10 nm thick, it intimately matches the roughness or smoothness of the FTO and ITO, respectively, resulting in many more nucleation sites on ITO, as evidenced by the larger number of grains seen particularly in Figure S6.1D. It is likely possible to reoptimize the rates during deposition to correct for this difference in nucleation and recover the higher performance seen on FTO/C_{60}.

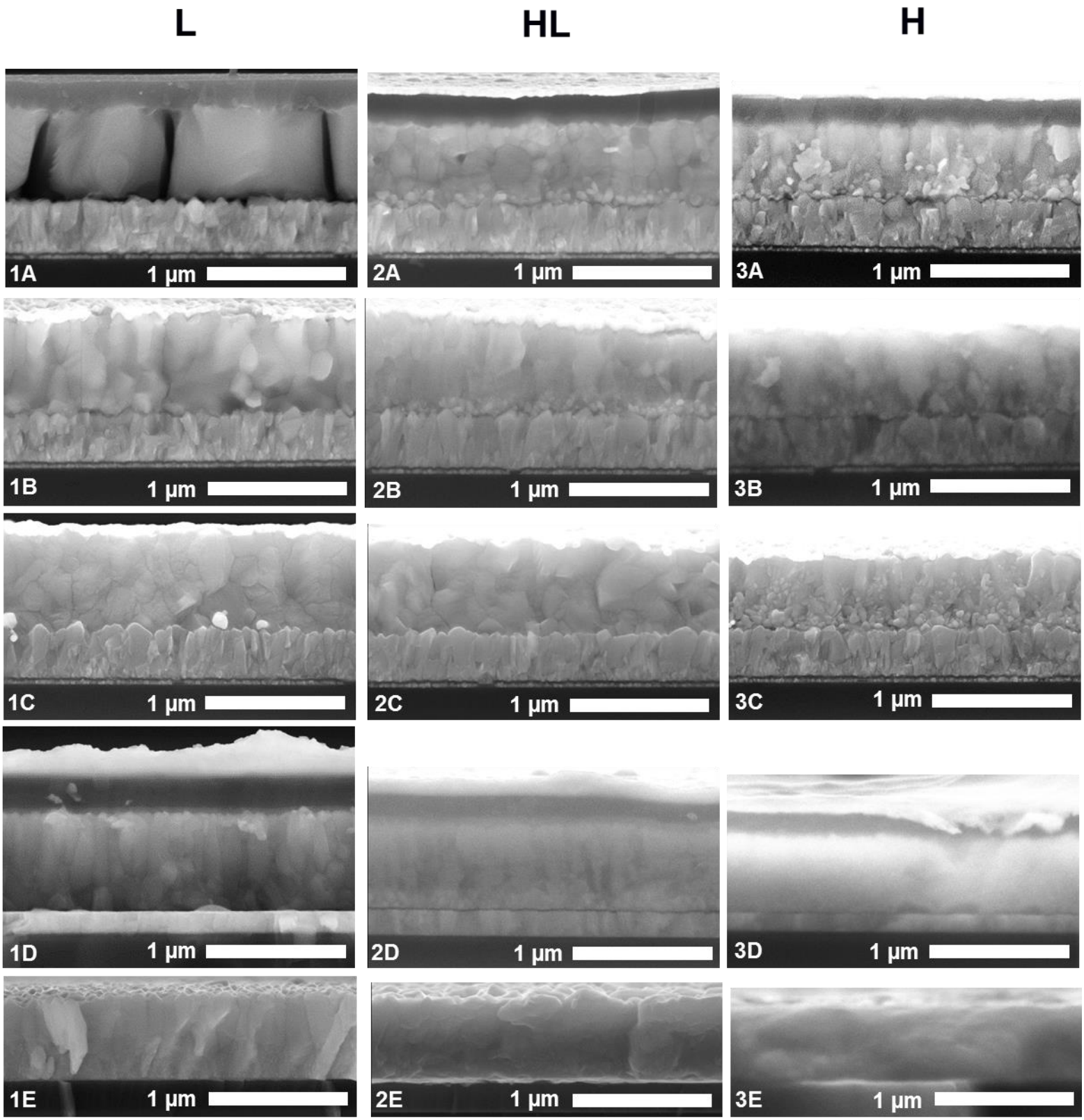

Figure S6: Cross-sectional scanning electron microscope images of co-evaporated $CH_3NH_3PbI_3$ ($MAPbI_3$) devices deposited at 3 different substrate temperature conditions L (column **1**),HL (column **2**), H (column **3**), as described in the main text. The rows correspond to the different substrates they are deposited on. **A:** FTO/C_{60}, **B:** FTO/Poly-TPD, **C:** FTO, **D:** ITO/C_{60}, **E:** crystalline silicon

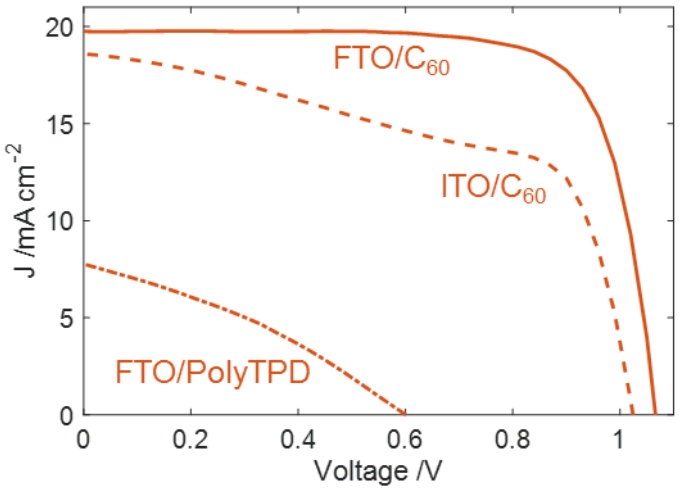

Figure S7: J-V curves of co-evaporated $CH_3NH_3PbI_3$ ($MAPbI_3$) devices grown at substrate temperature 23 °C on different substrates, namely fluorine-doped tin oxide (FTO)/C_{60}, Indium tin oxide (ITO)/C_{60}, FTO/PolyTPD. The device grown on FTO/C_{60} is the one labelled "H" elsewhere.

3. X-ray diffraction measurements and analysis

X-ray diffraction measurements were taken using a Panalytical X'pert poweder diffractometer equipped with a copper x-ray source (Cu-Kα set to 40 kV and 40 mA).

The spectra were then corrected for tilt by shifting the x-axis such that the reference FTO (110) peak sits at 2θ = 26.583° [4].

The background was then removed by fitting a 6th order polynomial to the entire spectrum.

The full width at half-maximum (FWHM) for the perovskite peaks was determined by fitting a pseudo-Voigt function to specific peaks following the formula used in [5]. In the case of HL, where a shoulder appears on the (110), (220), and (130) peaks from the tetragonal phase, a double pseudo-Voigt function is fit, and the FWHM value presented corresponds to that of the higher angle, higher intensity peak.

To determine the instrument broadening, we applied the same procedure as above to a reference silicon sample. We then plotted FWHM against 2θ, then fit a quadratic of the form $y = ax^2 + c$ to this data to determine the instrument broadening at any scattering angle. This plot and fit is shown in Figure S8. Using the fitted curve we determined the instrument broadening value at the peak position of the perovskite (130) peak of sample L, $2\theta = 31.85°$. At this angle, the instrument broadening was found to be 0.0628°.

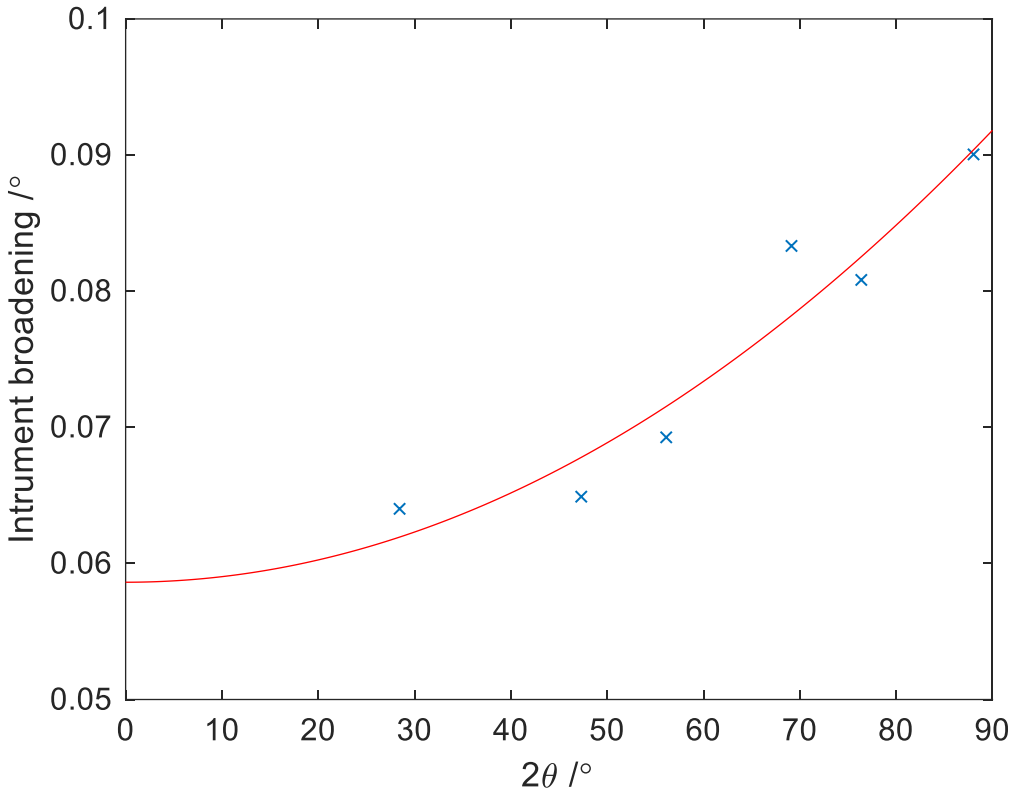

Figure S8: Instrument response curve for the x-ray diffractometer used in this study. The blue crosses represent the full-width at half maximum values for a reference Si sample, while the red curve represents the fitted polynomial.

4. Champion device

Careful optimisation of the substrate temperature control method at room temperature yielded a champion device when the thickness was increased slightly to 600 nm. This device was produced at substrate temperature 20°C. The champion JV efficiency achieved was 18.3%, with the stabilised efficiency after 50s being 17.5%. The device showed some light soaking, with the initial stabilised measurement only yielding 17.3%. The champion scan is the final of 14 successive JV scans, and the champion stabilised efficiency was measured straight after using the voltage at maximum power point measured during the scan. Figure S9 shows the champion JV curve, the stabilised efficiency and current measurements, as well as the spread in measured stabilised efficiencies across eight devices made in the same batch.

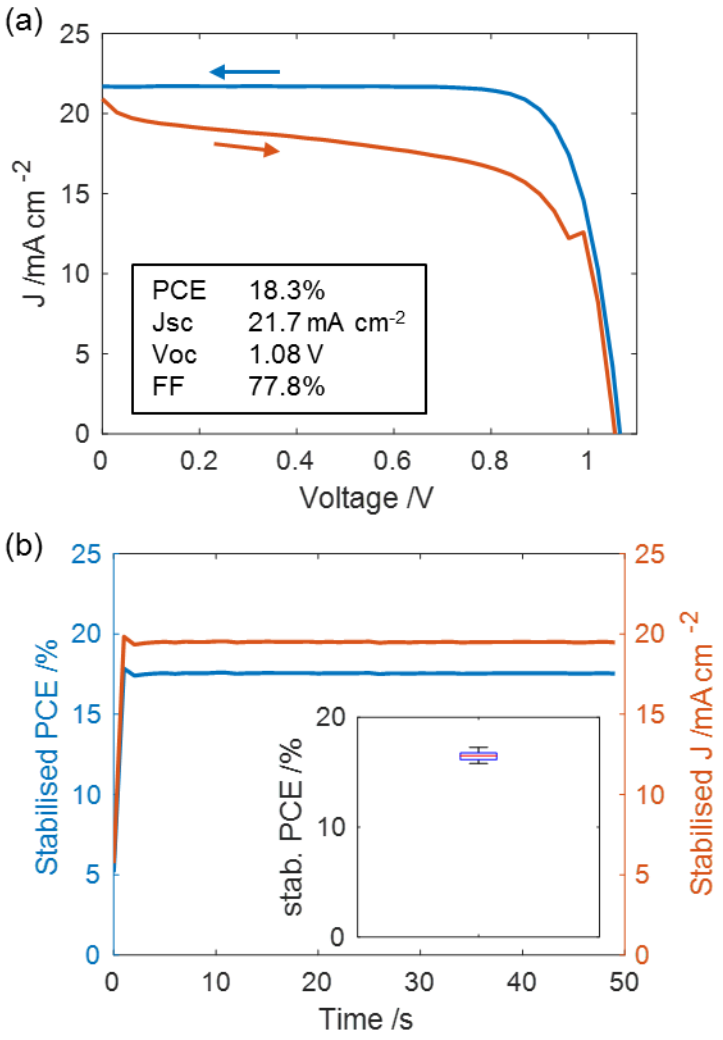

Figure S9: (a) J-V curve of the champion device, with the reverse scan (V_{OC} to J_{SC}) in blue, and the forward scan (J_{SC} to V_{OC}) in red. The inset is a table of the J-V characteristics taken from the reverse scan **(b)** Stabilised power conversion efficiency (PCE) and current at max power point voltage over 50 seconds. The inset represents the stabilised PCE data for the devices made in the batch that included the champion device.

5. Optical characterization

5.1 External quantum efficiency

External quantum efficiency (EQE) measurements (Figure S10) were taken using a modified Fourier transform photocurrent spectrometer based on a Bruker Vertex 80v Fourier Transform Interferometer, using a near-infrared source. The recorded spectra were calibrated using a Newport-calibrated reference silicon solar cell of known EQE value. The devices measured were the same as for the JV characterisation, with individual pixels singled out with a mask. The active area of the devices was still defined as 0.0919 cm^2, as per the rear gold electrode.

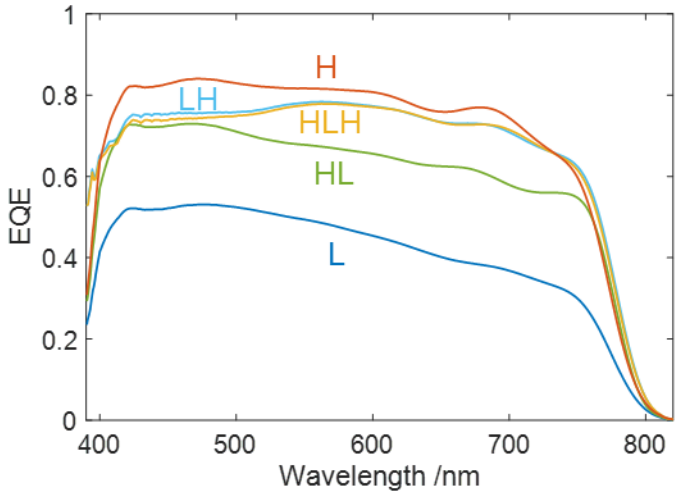

Figure S10: External quantum efficiency (EQE) of co-evaporated $CH_3NH_3PbI_3$ ($MAPbI_3$) devices deposited at 5 different substrate temperature conditions L,LH,HL,HLH,H, as described in the main text.

5.2 Urbach energy

Urbach energy (E_U) measurements were taken on the same setup as the EQE, using a 720 nm low-pass filter, such that the absorption band edge could be measured at a much higher sensitivity. The single exponential $y = e^{\frac{(x-a)}{E_U}}$ was fitted to the data in the region near the band edge to obtain E_U. Three measurements were taken per sample to get an average, with the error bars reflecting the random error in the mean.

5.3 Absorptance and internal quantum efficiency

The absorptance of the full devices was calculated from the reflection and transmission data of the full devices, using the formula $A_p = 1 - R - T$, where *R* and *T* are the reflection and transmission of full devices, respectively. The internal quantum efficiency (IQE) was then calculated from the absorptance and EQE using the formula $IQE = \frac{EQE}{A_p}$. IQE represents the probability of a photon leading to the collection of charge carriers once it has been absorbed by the device, i.e. the probability that the charge carriers generated by a photon of specific wavelength are collected. Absorptance is shown in Figure S11, with IQE shown in the main text Figure 3b.

5.4 Absorbance

Figure S12 shows the absorbance of bare $MAPbI_3$ devices after removal of the Au and spiro layer, grown on FTO/C_{60} at various substrate temperatures matching the terminology from the main text. Transmission and reflection measurements were taken on the same setup as the EQE; the formula used to calculate absorbance from transmission was $A_b = log_{10}\left(\frac{1-R}{T}\right)$ where *R* is the amount of light reflected off the sample and *T* is the amount of light transmitted through the sample.

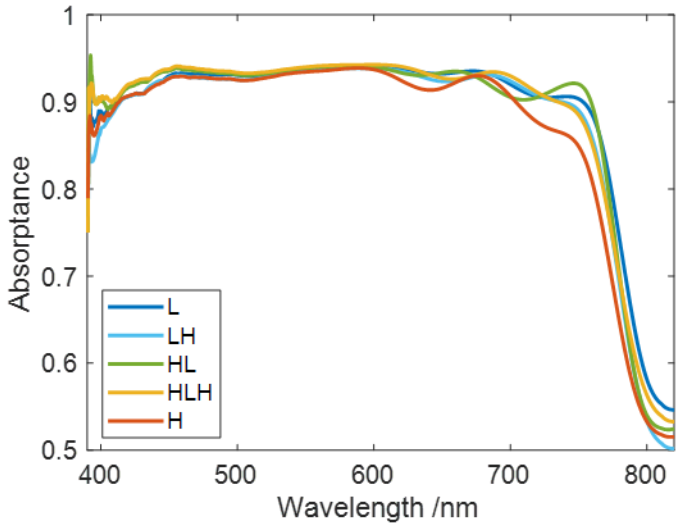

Figure S11: Absorptance of co-evaporated $CH_3NH_3PbI_3$ ($MAPbI_3$) devices deposited at 5 different substrate temperature conditions L,LH,HL,HLH,H, as described in the main text.

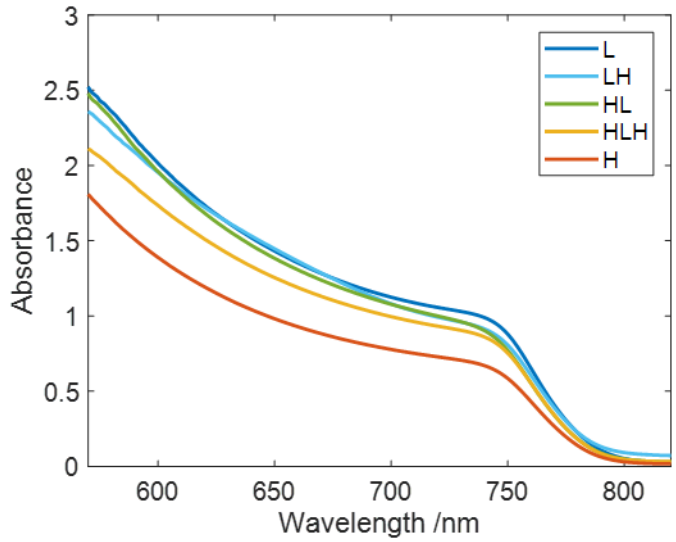

Figure S12: Absorbance of co-evaporated $CH_3NH_3PbI_3$ ($MAPbI_3$) thin films on FTO/C_{60}, deposited at 5 different substrate temperature conditions L,LH,HL,HLH,H, as described in the main text.

5.5 Integrated current from EQE

Using the Sun's known irradiance per wavelength for AM 1.5 it is possible to calculate the number of photons incident per wavelength on the solar cell. This then allows us to calculate the total current generated by the cell from the EQE by integrating over the current generated per wavelength, as shown in Figure S13.

(a)

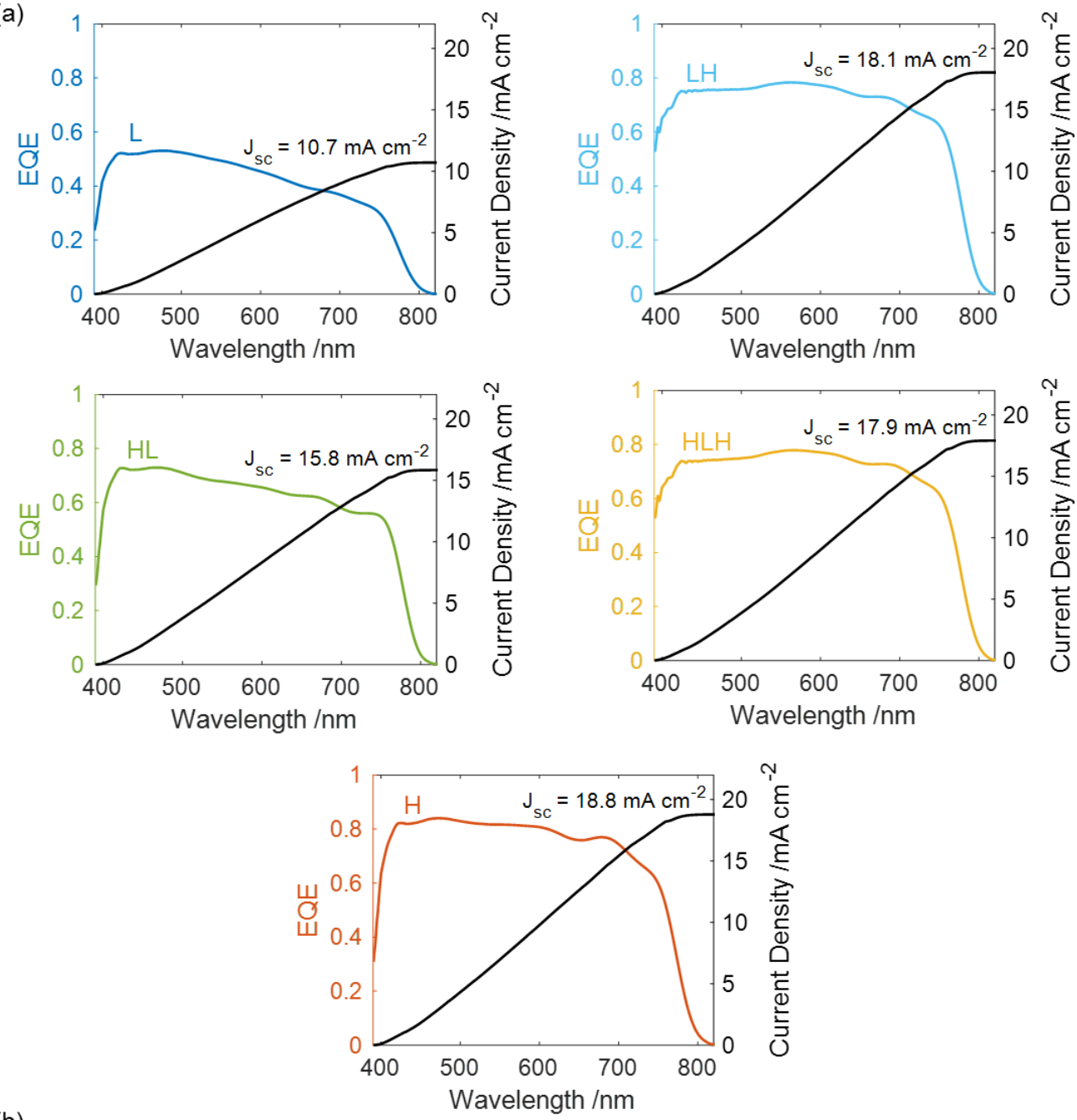

(b)

Device	J-V J_{SC} /mA cm^{-2}	EQE J_{SC} /mA cm^{-2}	J_{SPO} /mA cm^{-2}
L	14.1	10.7	11.2
LH	17.2	18.1	14.0
HL	16.9	15.8	12.8
HLH	16.5	17.9	11.3
H	19.5	18.8	17.0

Figure S13: (a) External quantum efficiency (EQE) measurements along with the cumulative current extracted over the EQE spectrum, as measured from the champion devices deposited at 5 different substrate temperature conditions L,LH,HL,HLH,H, as described in the main text. (b) Comparison of current extracted from the devices from the J-V scan (average of forward and reverse), the EQE spectrum, and the steady-state current density measured after 50s of constant operation at applied bias corresponding to the maximum power point, as determined by the J-V scan (J_{SPO}).

5.6 Optical pump THz probe spectroscopy

Optical-pump THz-probe spectroscopy (OPTPS) was used to measure transient absorption spectra, and hence extract the lateral charge carrier mobilities of samples grown on z-cut quartz (Figure S14). Because the samples are deposited on a different substrate, it is possible that the morphology is also different from devices grown on FTO/C_{60}. The samples grown at - 5 °C and 23 °C should give an indication of the charge carrier mobilities in L and H, respectively, the extremes of performance.

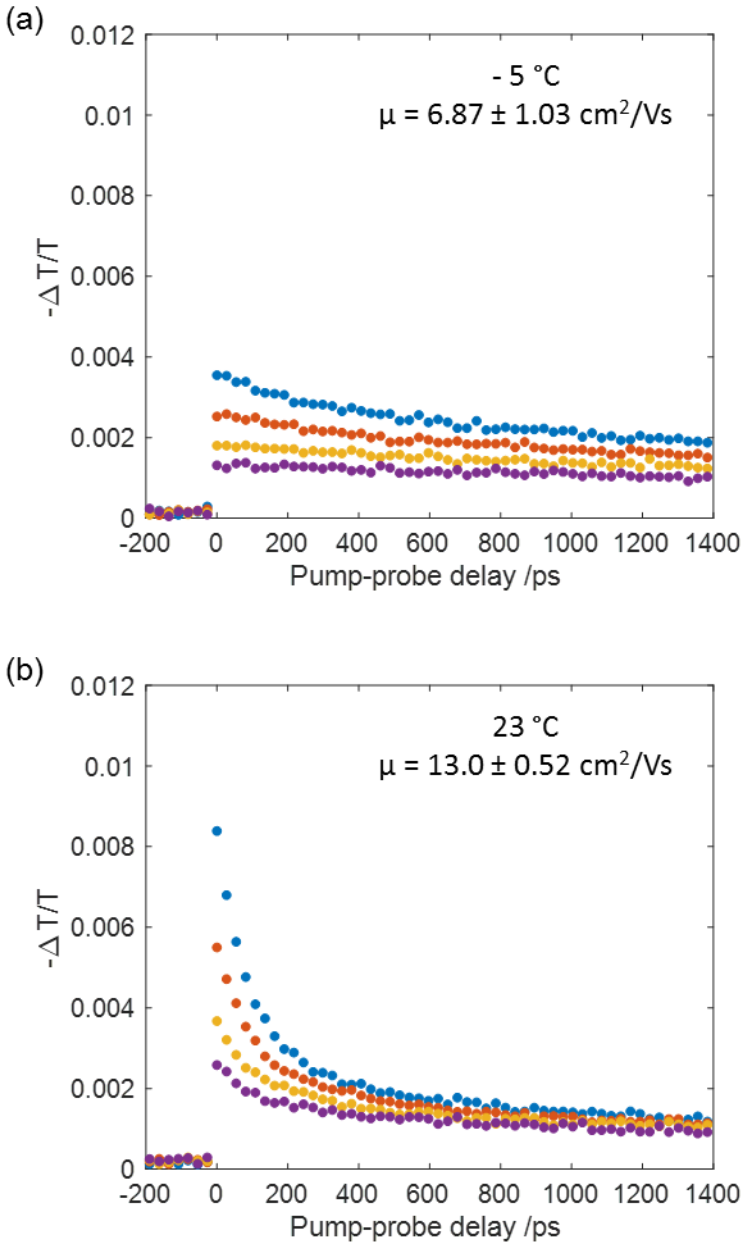

Figure S14: OPTPS measurements of bare $CH_3NH_3PbI_3$ ($MAPbI_3$) films grown on quartz at different substrate temperatures **(a)** -5 °C **(b)** 23 °C as measured at different photoexcitation fluences ranging from 6 (purple) to 22 (blue) $\mu J/cm^2$. The mobility values were extracted at the peak of the transient absorption spectra, which is before the charge-carrier recombination begins.

5.7 Steady-state photoluminescence

We performed steady-state pholomunescence (PL) measurements on the full devices deposited on FTO/C_{60} after removal of the gold and spiro layer, as shown in Figure S15. These measurements were taken by illuminating the samples with a 398 nm picosecond pulsed diode laser (PicoHarp, LDH-D-C-405M) operated under a continuous wave regime, at a power of 1 mW. The PL emitted by the films was coupled into a grating spectrometer (Princeton Instruments, SP-2558), and measured using and iCCD (PI-MAX4, Princeton Instruments).

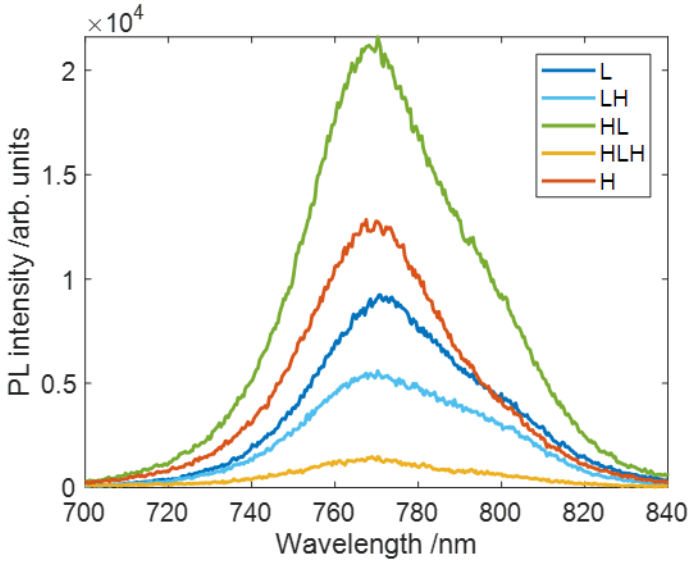

Figure S15: Steady-state photoluminescence of co-evaporated $CH_3NH_3PbI_3$ ($MAPbI_3$) thin films on FTO/C_{60}, deposited at 5 different substrate temperature conditions L,LH,HL,HLH,H, as described in the main text.

5.8 Time-resolved photoluminescence

To get a more complete overview of the optoelectronic properties of the films, we performed time correlated single photon (TCSPC) experiments on bare films grown on z-cut quartz (Figure S15). As with the OPTPS data, it is possible that the different substrate leads to a different morphology, but the films shown here, grown at substrate temperature -5 °C and 23 °C, should give an indication of the material properties of L and H, respectively. Contrary to what the device data suggests, the low temperature film can be seen to have a longer charge carrier lifetime. This can be resolved by the work of Chirvony et al., [6] who showed that the short lifetimes generally observed in vacuum processed metal halide perovskite films are due to fast diffusion of the photogenerated carriers to the interfaces. As such, the longer photoluminescence lifetimes of the low temperature film could indicate poorer diffusion of the charge carriers in this material, and hence worse performance. Possible further work to get around the issue of spatial charge separation includes transient photovoltage, though at the moment more work is needed to disentangle the effects of ion migration on this measurement technique. [7]

The TCSPC data was measured by a photon-counting detector (PDM series from MPD), using a PicoHarp300 TCSPC event timer to control its timing. The samples were photoexcited using a 398 nm picosecond pulsed diode laser (PicoHarp, LDH-D-C-405M) with excitation fluence around 400 nJ/cm^2 and repetition rate 5 MHz, and the counts collected at 768 nm using a grating spectrometer (Princeton Instruments, SP-2558).

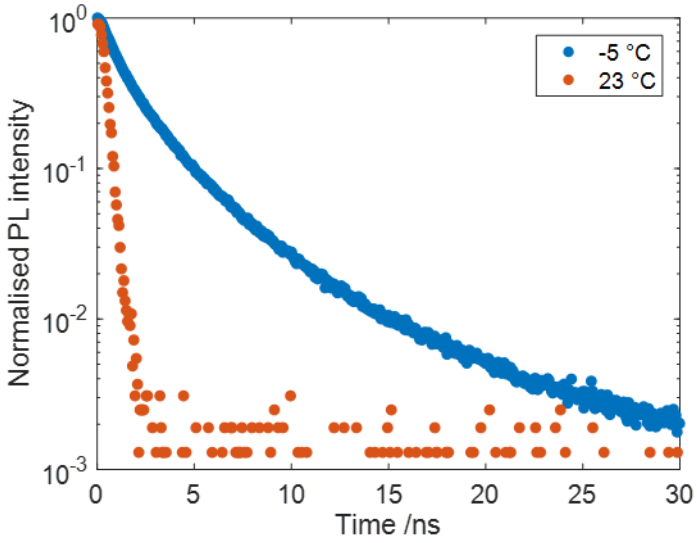

Figure S16: Time correlated single photon counting (TCSPC) trace of bare co-evaporated $CH_3NH_3PbI_3$ ($MAPbI_3$) thin films deposited on quartz at different substrate temperatures, namely -5 °C (blue dots) and 23 °C (red dots)

6. Effect of changing MAI flux

To differentiate between effects of temperature and stoichiometry, we made additional devices where we changed the MAI flux while keeping the PbI_2 rate constant.

6.1 Increasing MAI flux at substrate temperature 23 °C

One of the differences between L and H is stoichiometry, as H shows an excess of crystalline PbI_2. It stands to reason to wonder whether the morphological differences arise simply due to stoichiometry. We hence increased the MAI flux at substrate temperature 23 °C to see whether we could replicate the large grains seen in L. As shown in Figure S16, we found that we were unable to do so, even when increasing the amount of MAI evaporated by 90% as measured by the final weight in the crucible (H2), at which point there was no sign of any unreacted crystalline PbI_2 in the XRD pattern. Instead, it looks like increasing MAI leads to the disappearance of the small bright grains seen along the otherwise columnar grains, pointing to those grains being linked to excess PbI_2. Performance of the devices remained relatively unchanged, with a small increase in J_{SC} being balance by a small decrease in V_{OC}.

6.2 Decreasing MAI flux at low substrate temperature

Conversly, we find that when decreasing the MAI at low temperature, we do recover the morphology seen at room temperature, with a scattering of smaller grains on more columnar grains, indicating that stoichiometry does play a role in the resulting morphology (Figure S17). Interestingly, the performance of H is only recovered when the initial interface is grown at room temperature (LH1 and LH2). The substrate temperature used to grow these films was the following: L1, like L, was deposited entirely at -2 °C. HL1 and HL2 followed the same temperature variation as HL, with the exception that HL1 only went down to 0 °C rather than -2 °C.

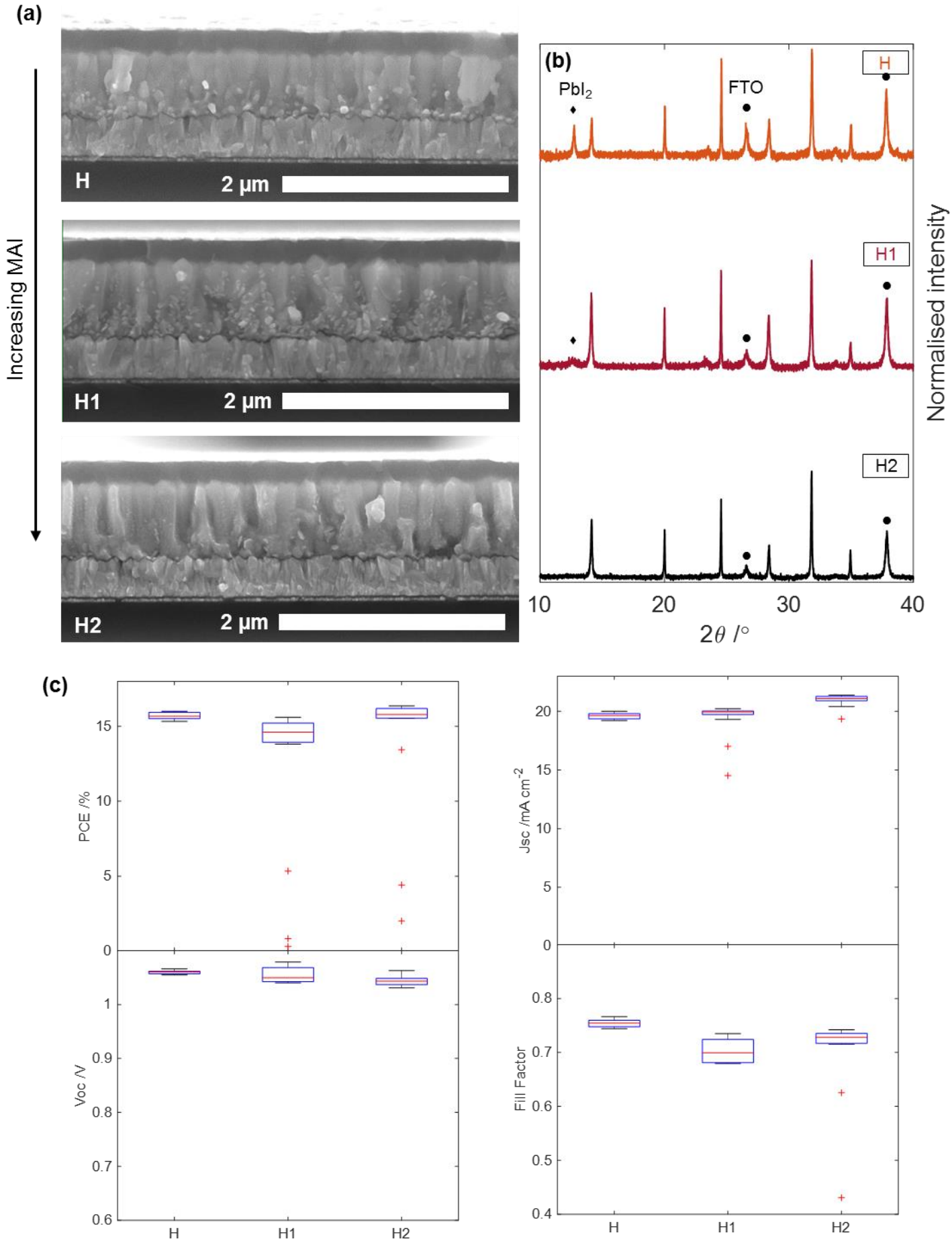

Figure S17: (a) cross-sectional SEM images of $CH_3NH_3PbI_3$ ($MAPbI_3$) films grown at substrate temperature 23°C with increasing MAI flux (MAI = CH_3NH_3I). H is the same sample show in the main text. H1 and H2 were deposited by evaporating 30% and 90% more MAI as measured from the weight lost during the evaporation. **(b)** XRD patterns for the corresponding devices. The diamonds denote the PbI_2 peak at 12.7°, the circles the FTO peaks. All other peaks are perovskite peaks. **(c)** J-V characteristics for the corresponding devices.

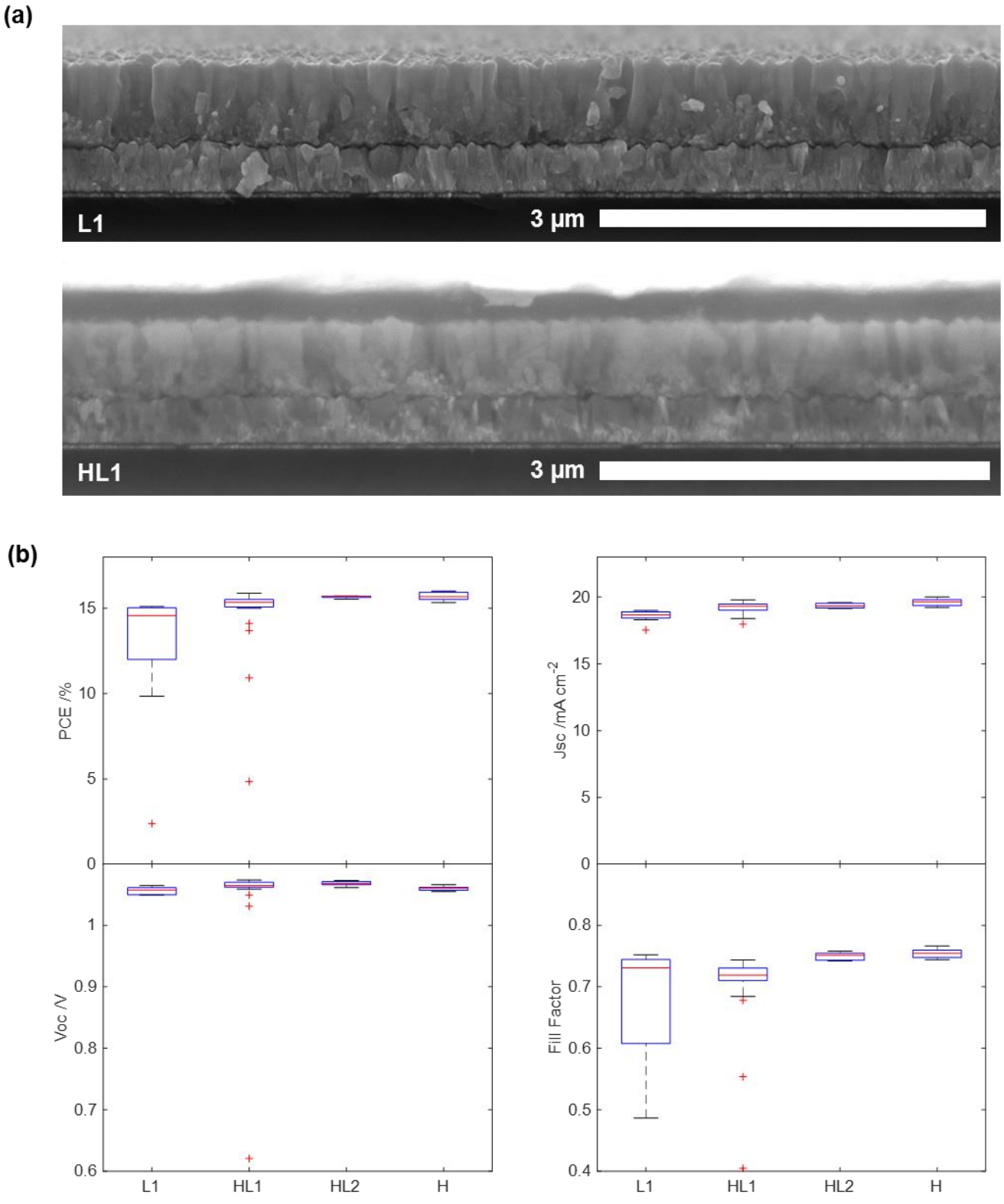

Figure S18: (a) cross-sectional SEM images of $CH_3NH_3PbI_3$ ($MAPbI_3$) films grown at various substrate temperatures, as described previously, with reduced MAI flux (MAI = CH_3NH_3I). **(b)** J-V characteristics for the corresponding devices. H is the same device as presented in the main text.

7. Increasing the substrate temperature above 23 °C

We briefly investigated the effects of increasing the substrate temperature above 23 °C, but found that the performance drops of after 23 °C, as shown in Figure S18. It is worth noting that we did not increase the MAI flux to balance the reduced MAI adsorption, but the more detailed study done by Kottokkaran et al. shows that the performance never fully recovers even when increasing the MAI flux to account for this [8].

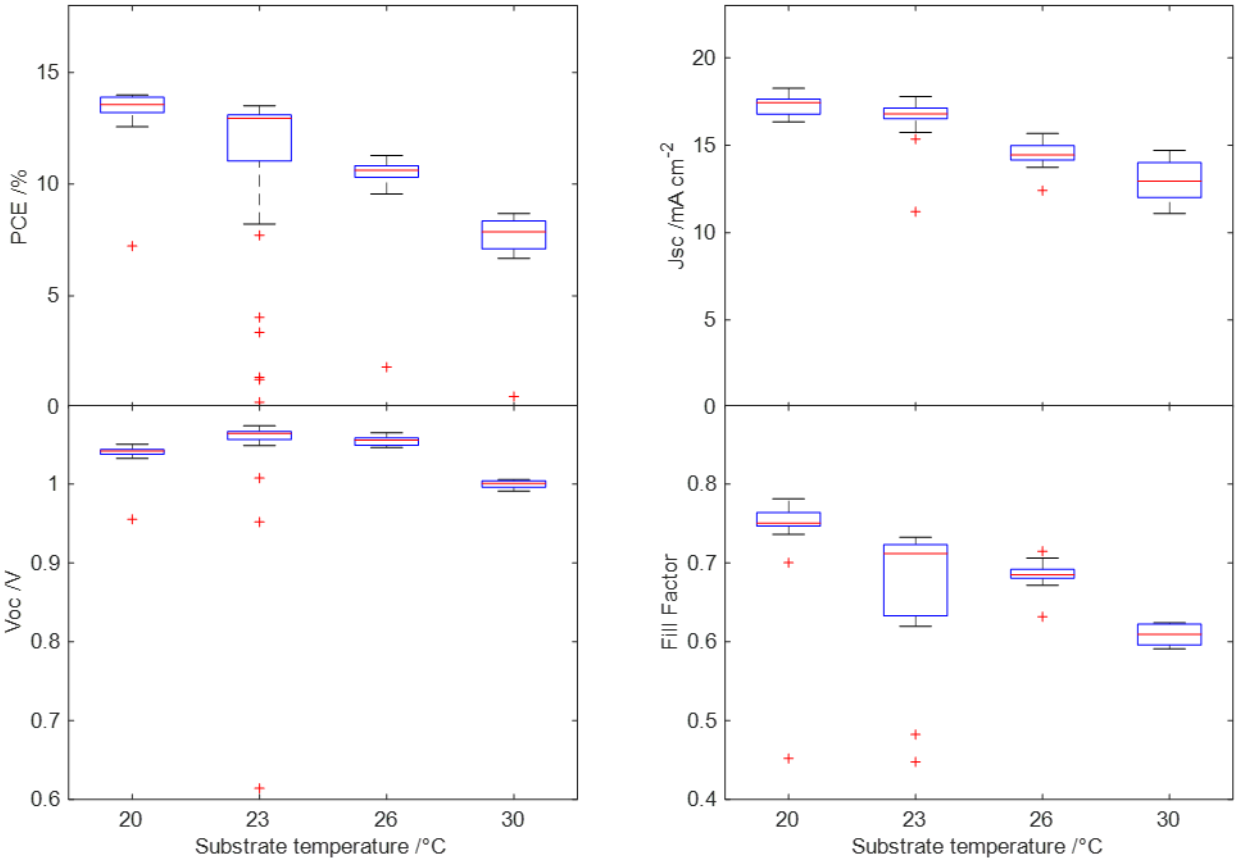

Figure S19: J-V characteristics for $CH_3NH_3PbI_3$ ($MAPbI_3$) devices grown at the same MAI flux (MAI = CH_3NH_3I) but different substrate temperature

8. Substrate rate control

We found substrate rate control to be a very reproducible method of growing films, particularly offering consistency across different batches of MAI made through different methods. Indeed, we found the substrate rate to be consistent even when the sticking coefficient of the MAI varied significantly. We obtained similar results with similar substrate rates for Greatcell MAI which doesn't stick on its own at all on quartz microbalances, and a homemade MAI that has much better adsorption on quartz microbalances, as shown in Figure S19. The table shows the raw (untooled) data from the quartz microbalances near the MAI source, the PbI_2 source, and the substrate, respectively, for these two depositions. It shows how similar the amount of material deposited near the substrate is even though the amount measured by the sensor near the MAI source is vastly different, and hence how the substrate rate is independent of the sticking rate of the MAI on its own because of how significant of an effect the presence of PbI_2 has.

(a)

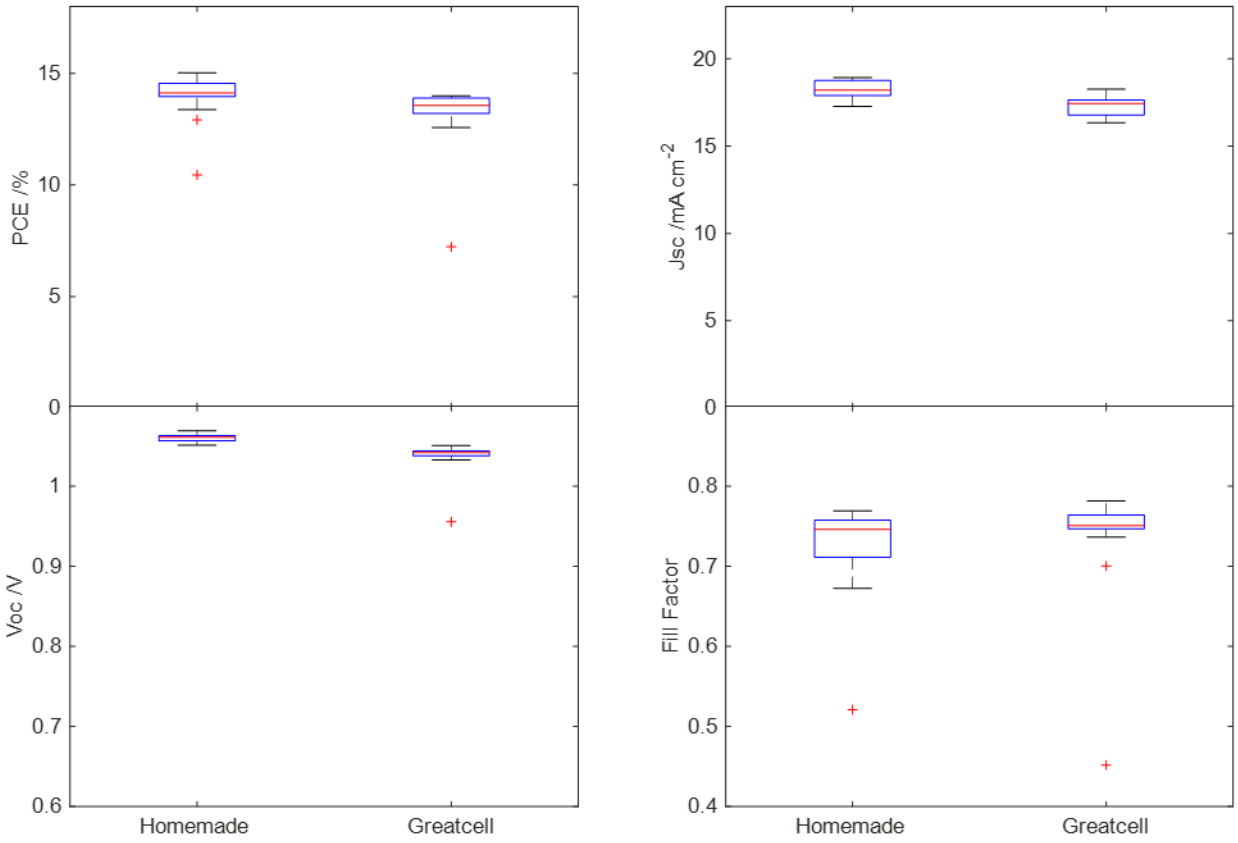

(b)

MAI supplier	Final thickness from raw (untooled) sensor data /arb. units		
	MAI sensor	**PbI_2 sensor**	**Substrate sensor**
Homemade	34.28	25.16	30.07
Greatcell	0.8543	25.35	31.24

Figure S20: (a) J-V characteristics for $CH_3NH_3PbI_3$ ($MAPbI_3$) devices grown using homemade MAI and Greatcell MAI **(b)** Final thicknesses as measured from the raw (untooled) sensor data for the three sensors in the chamber

References

[1] M. Yang, Y. Zhou, Y. Zeng, C.-S. Jiang, N. P. Padture and K. Zhu, "Square-Centimeter Solution-Processed Planar CH3NH3PbI3 Perovskite Solar Cells with Efficiency Exceeding 15%," *Adv. Mater.,* vol. 27, p. 6363, 2015.

[2] H. Yuan, E. Debroye, K. Janssen, H. Naiki, C. Steuwe, G. Lu, M. Moris, E. Orgiu, H. Uji-i, F. D. Schryver, P. Samorì, J. Hofkens and M. Roeffaers, "Degradation of Methylammonium Lead Iodide Perovskite Structures through Light and Electron Beam Driven Ion Migration," *J.Phys.Chem.Lett.,* vol. 7, p. 561, 2016.

[3] M. U. Rothmann, W. Li, Y. Zhu, A. Liu, Z. Ku, U. Bach, J. Etheridge and Y.-B. Cheng, "Structural and Chemical Changes to CH3NH3PbI3 Induced by Electron and Gallium Ion Beams," *Adv. Mater.,* vol. 30, p. 1800629, 2018.

[4] S. A. Yousif and J. M. Abass, "Structural, Morphological and Optical Characterization of SnO2:F thin films prepared by Chemical spray Pyrolysis," *Int. Lett. of Chem., Phys. and Astr.,* vol. 13, p. 90, 2013.

[5] P. Thompson, D. E. Cox and J. B. Hastings, "Rietveld refinement of Debye-Scherrer synchrotron X-ray data from Al2O3," *J. Appl. Cryst.,* vol. 20, p. 79, 1987.

[6] V. S. Chirvony, K. S. Sekerbayev, D. Pérez-del-Rey, J. P. Martínez-Pastor, F. Palazon, P. P. Boix, T. I. Taurbayev, M. Sessolo and H. J. Bolink, "Short Photoluminescence Lifetimes in Vacuum-Deposited CH3NH3PbI3 Perovskite Thin Films as a Result of Fast Diffusion of Photogenerated Charge Carriers," *J. Phys. Chem. Lett.,* vol. 10, p. 5167, 2019.

[7] D. Walter, A. Fell, Y. Wu, T. Duong, C. Barugkin, N. Wu, T. White and K. Weber, "Transient Photovoltage in Perovskite Solar Cells: Interaction of Trap-Mediated Recombination and Migration of Multiple Ionic Species," *J. Phys. Chem. C,* vol. 122, p. 11270, 2018.

[8] R. Kottokkaran, H. A. Gaonkar, H. A. Abbas, M. Noack and V. Dalal, "Performance and stability of co-evaporated vapor deposited perovskite solar cells," *J Mater Sci: Mater Electron,* vol. 30, p. 5487, 2019.